ADVANCED ELECTRONIC MATERIALS
www.advelectronicmat.de

Boosted Charge-Carrier Transport in Triple-Cation Perovskites by Ultrasonic Vibration Post Treatment

Yuzhuo Wang, Mohammad-Reza Ahmadian-Yazdi, Yangyang Ni, Yexin Jiang, Morteza Eslamian, Zuanming Jin, and Qianli Chen**

Ultrasonic vibration imposed on the substrate of a drying perovskite solution film has previously been proposed as a nearly annealing-free method to improve film quality and thus the photovoltaic performance for perovskite solar cells. However, an in-depth understanding of the underlying mechanism of the improved film quality via ultrasonic vibration is still lacking. In this work, the effects of substrate vibration post treatment on the carrier lifetime and mobility are studied in triple-cation perovskite films. With 80 s of annealing-free vibration, the perovskite film demonstrates much stronger photoluminescence intensity and much longer carrier lifetime up to 2.634 µs, 2 orders of magnitude longer than that of the thermal annealed films. Optical pump terahertz probe spectroscopy reveals that the charge-carrier mobility increases to 121 ± 44 $cm^2 V^{-1} s^{-1}$ when subjected to 80 s vibration followed by annealing. Such mobility is about 80 ± 40 $cm^2 V^{-1} s^{-1}$ higher than that of other polycrystalline organic–inorganic hybrid perovskite thin films of similar composition. The diffusion length is improved to nearly 1.5 times. The new understanding on the vibration-induced charge-carrier transport properties paves the way for the application of ultrasonic vibration toward the performance improvement of perovskite-based electronic devices.

1. Introduction

In the past decade, we have witnessed an intensive growth of interest in metal halide perovskites (MHPs). The general chemical formula of MHPs is ABX_3, where A stands for cations like methylammonium (MA or CH_3NH_3), B stands for divalent metallic cations (Sn, Pb, or Ti), and X stands for halide anions such as iodide (I), bromide (Br), or chloride (Cl). Since 2009 when Miyasaka and co-workers[1] first applied MHP to solar cells and realized a power conversion efficiency (PCE) of 3.8%, rapid improvements in PCE (currently up to 25.5%[2]) have been achieved. Because of the tunable optical and electronic properties of MHPs combined with facile processing procedures,[3] applications of MHPs are no longer limited to solar cells, but have quickly extended to light-emitting diodes,[4,5] photodetectors,[6–9] amplified spontaneous emission of lasers,[10–13] field-effect transistors,[14,15] etc.

Among all possible combinations in the category of perovskite materials, triple-cation perovskites, consisting of cesium (Cs^+), methylammonium (MA^+), and formamidinium (FA^+) cations at A-site in the ABX_3 structure, have gained tremendous attention. Saliba et al.[16] demonstrated that triple-cation perovskites show outstanding stability in photovoltaic devices and reproducibility during the fabrication process. By introducing a small amount of Cs^+ in MHPs, unstable yellow phase is effectively suppressed,[16] allowing the formation of a more stable black perovskite phase, which resists against humidity and temperature. The performance of solar cells employing the triple-cation perovskites has improved rapidly in the last 5 years.[17–20] Zhou and co-workers[20] have obtained an outstanding PCE of 21.46% by simultaneously passivating both anion and cation vacancies in the perovskite layer, and the device preserves 90% of the original PCE after 1000 h of operation. Recently, tandem devices combining triple-cation perovskites and *c*-Si have reached a PCE of >25%.[21]

To fabricate solar cells with desirable performance, it is of vital importance to make high-quality perovskite films by controlling the crystallization process. By doing so, the non-radiative recombination is suppressed. Such positive effects have been reported by Gao et al. in the relevant morphology studies on porphyrin-based organic photovoltaics.[22,23] In this regard, multiple strategies have been developed. The traditional methods to control crystallization require a final step by annealing and drying the liquid films at temperatures ranging from 70 to 150 °C, to form a solid film.[24–28] Despite the simplicity of this method, annealing tends to yield films with rough surface and pores, and defects in the crystalline structure.[29] An alternative approach is to partially or fully replace annealing with ultrasonic vibration with nanoscale amplitudes imposed on the thin liquid films during drying.

Y. Wang, M.-R. Ahmadian-Yazdi, M. Eslamian, Q. Chen
University of Michigan–Shanghai Jiao Tong University Joint Institute
Shanghai Jiao Tong University
Shanghai 200240, China
E-mail: qianli.chen@sjtu.edu.cn
Y. Ni, Y. Jiang, Z. Jin
Shanghai Key Lab of Modern Optical Systems
Terahertz Technology Innovation Research Institute
Terahertz Spectrum and Imaging Technology Cooperative Innovation Center
University of Shanghai for Science and Technology
Shanghai 200093, China
E-mail: physics_jzm@usst.edu.cn
The ORCID identification number(s) for the author(s) of this article can be found under https://doi.org/10.1002/aelm.202101286.

DOI: 10.1002/aelm.202101286

Relevant theoretical studies on waves and vibration imposed on liquids are traced back to 1837 by Faraday.[30] The theory of thin liquid film evolution induced by vibration was gradually established by Kumar and Matar,[31,32] Matar et al.,[33] Shklyaev et al.,[34,35] Bestehorn,[36] Khan and Eslamian,[37] etc. Ultrasonic vibration has been imposed on perovskite thin films to obtain enhanced solar cell PCE.[38–40] Zabihi and co-workers manufactured flexible perovskite solar cells using ultrasonic vibration and achieved a champion PCE of 17.38%, which is competitive among the reported performance of flexible devices.[40] It was proposed that[41] the disturbance wave generated in the vibrating process could circulate the fluid particles throughout the liquid film, resulting in mixing of liquid solution in microscale and thus forming a uniform and homogeneous solid film upon drying. Compared to traditional high-temperature annealing that requires long duration, ultrasonic vibration has a better control of the evaporation rate.[42] The effect of acoustic vibration depends on the vibration power (wave amplitude), frequency, and duration.[43] Controlled imposed vibrations could create micromotions in the wet film and improve the uniformity and homogeneity of the ensuing solid film, both for passive and active thin-film coatings.[43] A systematic study was carried out to find optimum power and frequency of ultrasonic vibration on the perovskite films.[38] Ultrasonic vibration plays a crucial role in controlling the crystal size, growth rate, as well as improving the photovoltaic performance of such active thin films. In addition, Eslamian and co-workers have employed ultrasonic vibration as a completely annealing-free approach for perovskite solar cells.[42] Because ultrasonic vibration has the potential to make the fabrication process annealing free, the cost of manufacturing is expected to be decreased. Another study has shown that poly(3-hexylthiophene) (P3HT) :phenyl-C61-butyric acid methyl ester (PCBM)) polymer solar cells made with ultrasonic vibration on the spun-on poly(3,4-ethylenedioxythiophene) polystyrene sulfonate (PEDOT:PSS) layer become highly reproducible, which is another important step toward commercialization of the technology.[44] These studies have proved the feasibility for this method to be extended to mass production of solution-processed solar cells.

Although the aforementioned works have offered explanations on the effects of ultrasonic vibration on the film microstructure based on the theories of fluid mechanics, in-depth research on the vibration-induced properties of the photogenerated charge carriers that control the photovoltaic performance of perovskite solar cells is still limited. Xiong et al. reported that with annealing-free ultrasonic vibration, the charge-carrier lifetime of $(FAPbI_3)_{0.85}(MAPbI_3)_{0.15}$ perovskite films was prolonged to 51.23 ns, about 20 ns longer compared with the thermal annealed films.[39] In the present research, we study the influence of ultrasonic vibration time on charge-carrier lifetime, mobility, and diffusion length in triple-cation perovskite films. Photoluminescence (PL) and time-resolved photoluminescence (TRPL) are used to study the recombination of charge carriers in low charge-carrier density scenarios, and optical pump terahertz probe (OPTP) spectroscopy is used to study the behavior of charge carriers in the regime of high charge-carrier density within hundreds of picoseconds. The charge-carrier mobility is extracted using the Drude–Smith model. We show that the films treated with ultrasonic vibration exhibit improved charge-carrier lifetime, diffusion length, as well as mobility under various charge-carrier densities.

2. Results and Discussion

All perovskite films are prepared on *z*-cut quartz substrates for characterizations, and the detailed sample preparation procedures are described in the "Experimental Section." The nominal composition of our thin films is $Cs_{0.05}(MA_{0.17}FA_{0.83})_{0.95}Pb(I_{0.83}Br_{0.17})_3$. For convenience, we name these samples Vib-*x*, where "Vib" denotes "vibration" and *x* represents the time of ultrasonic vibration in seconds. After vibration, all Vib-*x* films were annealed for 45 min to evaporate the remaining solvents. For example, Vib-0 refers to thin film post-treated with vibration for 0 s, and annealing for 45 min. For comparison, another set of thin films were post-treated with vibration for 80 s and no annealing afterward (denoted as "annealing-free vibration"). The thicknesses for all thin films are 280 ± 10 nm, as determined in Figure S1 (Supporting Information). From the ultraviolet–visible absorption spectra in Figure S2 (Supporting Information), the bandgaps of films are found to be between 1.64 and 1.66 eV, as shown in Figure S3 (Supporting Information), consistent with a previous report.[3]

Steady-state PL is applied to study the optical emission process. As shown in **Figure 1**a, the PL intensity is significantly enhanced with the increasing vibration time, and reaches a maximum at 80 s. To demonstrate the potential of vibration on the photoluminescence of perovskites, Figure S4a (Supporting Information) compares the PL intensity of the films treated by annealing-free vibration and pure annealing, showing an enhanced emission of more than 2 orders of magnitude for the annealing-free vibration film. It is noticeable that the line shapes of all curves are visibly asymmetric. Therefore, we fitted each curve with two individual Gaussian functions, as shown in Figure S5 (Supporting Information). All fitting scenarios have a goodness exceeding 99.8%. We assign these two Gaussian functions as the contributions from emissions of free excitons at lower wavelength (pink) and trap states at higher wavelength (green),[45] because emission involving trap states within the bandgap is expected to have lower energy comparing to band-to-band transition from free excitons. The peak areas representing the PL intensity contributed by these two processes are shown as a function of the vibration time in the inset of Figure 1b. We observe an up to 35-fold increase for Vib-80 compared to Vib-0 in the emission from free excitons (pink), and around 10-fold increase in the emission from trap states (green). Such an increase indicates that with substrate vibration post-treatment, the process of carrier recombination has been effectively suppressed. To demonstrate the impact of vibration on the contribution from trap states within all emitted photons, we plot the area ratio of the green peaks to the overall PL spectra, as shown in Figure 1b, as a function of the vibration time. When the ultrasonic vibration is applied, the contribution from trap states has decreased from 42.4% for Vib-0 to around 30%, and such level remains relatively steady between Vib-20 and Vib-100. As a result of the enhanced contribution from free excitons, the PL spectra in Figure 1a show a blueshift in the

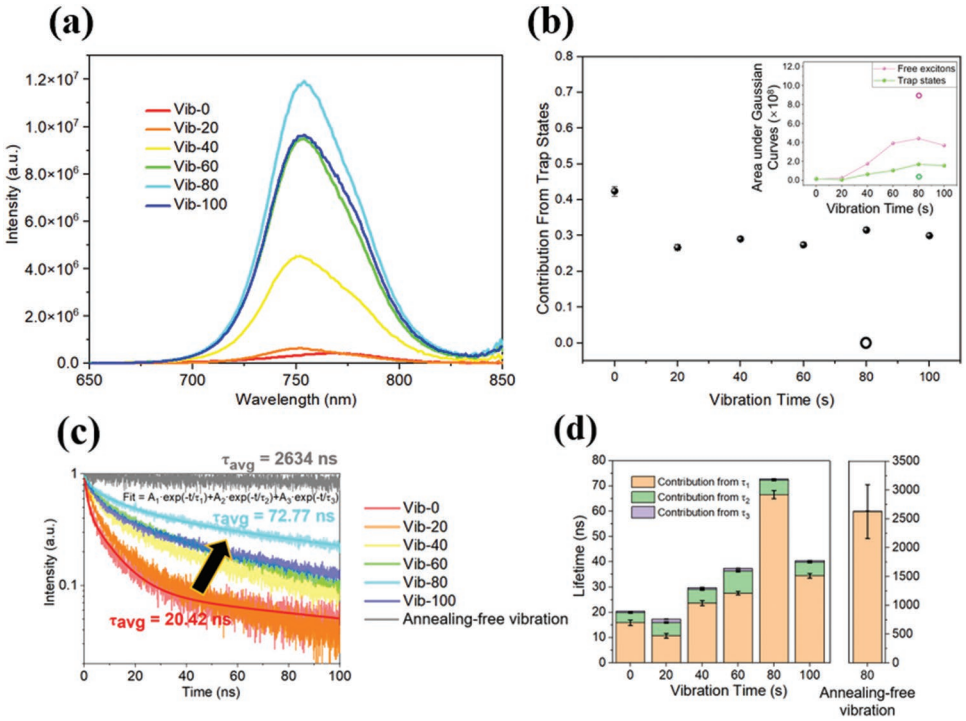

Figure 1. a) Steady-state PL spectra of perovskite films prepared with vibration time from 0 to 100 s followed by 45 min thermal annealing. b) The contribution of emission from trap states versus vibration time. Inset: Emission from free excitons (pink) and from trap states (green) versus vibration time. Closed circles: Vib-0 to Vib-100; open circles: annealing-free vibration. c) Normalized TRPL spectra of films. The red line refers to the fitted exponential decay curve for Vib-0, while the cyan line refers to the fitted exponential decay curve for Vib-80. d) Bar chart of average lifetime including contribution from τ_1, τ_2, and τ_3 for different vibration times.

peak from ≈763 to ≈754 nm when vibration is imposed. It is worth noting that the thin film processed with annealing-free vibration only shows the contribution from free excitons, as only one Gaussian curve centered at 742 nm fits the peak well with the fitting goodness R^2 of 99.9%, as shown in Figure S4b (Supporting Information). The area under the Gaussian curve in Figure S4b (Supporting Information) and the contribution of trap states are both demonstrated in Figure 1b as open circles. Therefore, for the annealing-free vibration film, the contribution from trap states is almost zero. This outstanding PL intensity demonstrates the potential of vibration to eliminate defects in the crystalline lattice, which are generated in the conventional annealing process. Our previous work has shown the crystallization of perovskites with uniform grain size within 2 min vibration.[42] We note that since the signals collected are those escaped from the sample surface, the level of trap states determined from PL merely comes from the top surface, which cannot be equalized to the level of entire perovskite layer. The accurate determination of the density of trap states requires further study.

Figure 1c displays the TRPL spectra for thin films prepared at various vibration times. The photoluminescence decay of another thin film treated with annealing-free vibration for 80 s is also included, shown as a gray curve. The normalized intensity, as a function of time elapse, is described by a triexponential function. All fitting curves show goodness R^2 over 98%, and compared with a biexponential function, the triple-term shows better accuracy and reduced standard error.[46] The average carrier lifetime is defined as $\tau_{avg} = (A_1\tau_1 + A_2\tau_2 + A_3\tau_3)/(A_1 + A_2 + A_3)$. The contributions of τ_1, τ_2, and τ_3 (that is, $A_1\tau_1$, $A_2\tau_2$, and $A_3\tau_3$, where $A_1 + A_2 + A_3 = 1$) are plotted in Figure 1d for different vibration times, and the fitting details are listed in Table S1 (Supporting Information).

Here we attribute the slow-decay component (τ_1) to radiative recombination from bulk perovskite, which dominates the contribution to the total lifetime. The two fast-decay components (τ_2 and τ_3) represent extrinsic trap-assisted and lattice periphery-confined recombination, respectively.[5,46] As shown in Figure 1d, because of the increase in contribution of τ_1 from 15.65 ns for Vib-0 to 66.59 ns for Vib-80, the average carrier lifetime increased from 20.42 ns to a maximum of 72.77 ns, which is nearly four times, while the variations of contributions of τ_2 and τ_3 are both within 4 ns for all samples. Notably, the carrier lifetime for the thin film treated with annealing-free vibration is 2.634 µs, 2 orders of magnitude longer than other films. The carrier lifetime in microsecond range is competitive among the previous reported triple-cation perovskite thin films.[47,48] Moreover, the contributions of τ_2 and τ_3 are almost negligible. According to the electron–hole radiative recombination and the effective PL lifetime equations under low-illumination condition,[49] the improved lifetime is correlated with the decreased carrier-trapping rate, which strongly depends on the quality of the thin film. Figure 1c indicates that the carrier trapping for thin film processed with annealing-free vibration is successfully suppressed. We also note that vibration time longer than 100 s introduces a detrimental effects (Section S11,

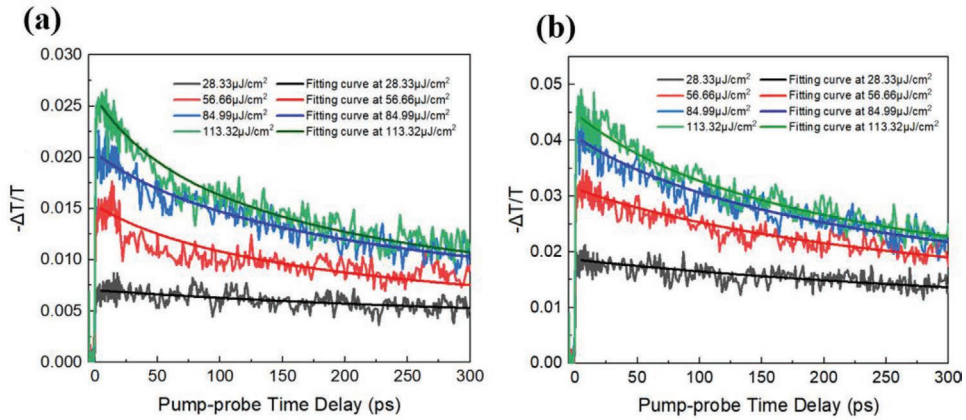

Figure 2. THz conductivity transients and fitting curves under four different fluences for a) Vib-0 and b) Vib-80.

Supporting Information), confirming that under the current processing condition, the longest charge-carrier lifetime was obtained using the vibration time of 80 s. Measuring the PL quantum efficiency will further establish the widespread utility of the substrate vibration post treatment for the solution-processed perovskite electronic devices. Based on our observations, we propose that optimizing the post-treatment process by developing annealing-free vibration or followed by a gentle annealing process may further extend the carrier lifetime, and deserves extensive studies in the future.

To investigate the effects of vibration on carrier mobility and diffusion length, we further measured the transient THz photoconductivity for Vib-0 and Vib-80 after photoexcitation at 400 nm. Although the annealing-free vibration film shows superior charge-carrier lifetime, previous studies have shown that solvent remains in the film even after 3 min of ultrasonic vibration.[42] Since the remaining solvent reduces the film conductivity greatly and forms intermediate phases with perovskite, we chose the annealed films Vib-0 and Vib-80 for the THz photoconductivity measurement. In **Figure 2**, four distinct excitation fluences are selected, ranging from 28.33 to 113.32 μJ cm^{-2}. The transient conductivity is probed by a THz radiation pulse as a function of pump–probe time delay, and the conductivity is originated from photoexcited charge carriers. Comparing Figure 2a and Figure 2b, we find that with 80 s vibration applied, the initial conductivity starts off at the first picoseconds almost doubled for each fluence, and the overall decay rate for Vib-80 decreases, as revealed by the slope difference from both subfigures at the same fluence. A full introduction of the recombination model and the fitting details for the recombination rates of charge carriers are provided in Section 7 (Supporting Information). The three recombination rate constants, k_1, $k_2\phi$, and $k_3\phi^2$, representing monomolecular, bimolecular, and Auger recombination rates, respectively, are obtained from a global fit for all fluences. The latter two terms represent the lower limits to the actual rates of recombination, where ϕ is the photon-to-charge branching ratio. As shown in **Table 1**, the three recombination terms are all decreasing for Vib-80, indicating that all recombination processes among charge carriers are effectively suppressed as vibration is applied.

To further determine the charge-carrier mobility, we conducted a time-domain spectroscopy (TDS) analysis at a fixed pump–probe delay time. TDS provides frequency-resolved complex conductivity spectra, as demonstrated in **Figure 3**. Here we set the delay time as 5 ps and the fluence as 113.32 μJ cm^{-2}. The experimental details for the TDS measurement and data analysis for photoconductivity are included in the Supporting Information. According to the Kramers–Kronig relations,[50] the real and imaginary parts of the photoconductivity $\Delta\sigma(\omega, \Delta t)$ can be derived through Fourier transform. As observed in Figure 3, for Vib-0 and Vib-80, both the real and imaginary parts of the photoconductivity slightly increase with frequency. All spectra are well-described by the Drude–Smith model.[51–54] This model describes the conduction of free charge carriers under long-range localization condition, with the following equation

$$\tilde{\sigma}_{DS}(\omega) = \frac{\varepsilon_0 \omega_p^2 \tau_s}{1 - i\omega\tau_s}\left(1 + \frac{c}{1 - i\omega\tau_s}\right) \quad (1)$$

where ε_0 is the permittivity of vacuum, ω_p indicates the frequency of plasma, and τ_s represents the momentum relaxation time. c is the localization degree parameter that describes the probability of a carrier maintaining its velocity during scattering. The value of c varies between −1 and 0, where $c = 0$ denotes full momentum randomized scattering (so Equation (1) becomes the classic Drude formula),[55] while a negative c means that the charge carrier undergoes preferential backscattering, i.e., localization, for example, when reaching the edge of a local potential well.[50] The mobility is calculated by the relation $\mu = e\tau_s/m^*$, where e is the elementary charge and m^* is the carrier effective mass.[56] Here we assume the carrier effective mass $m^* = 0.13m_e$ based on previous experiments

Table 1. Monomolecular (k_1), bimolecular ($k_2\phi$), and Auger ($k_3\phi^2$) recombination rates, fitted from the charge-carrier recombination model of thin films processed with different ultrasonic vibration times.

Vibration time [s]	k_1 [10^6 s^{-1}]	$k_2\phi$ [10^{-10} cm^3 s^{-1}]	$k_3\phi^2$ [10^{-28} cm^6 s^{-1}]
0	13.892 ± 0.195	9.379 ± 1.454	100.8 ± 7.561
80	8.131 ± 0.053	5.626 ± 1.062	33.59 ± 1.666

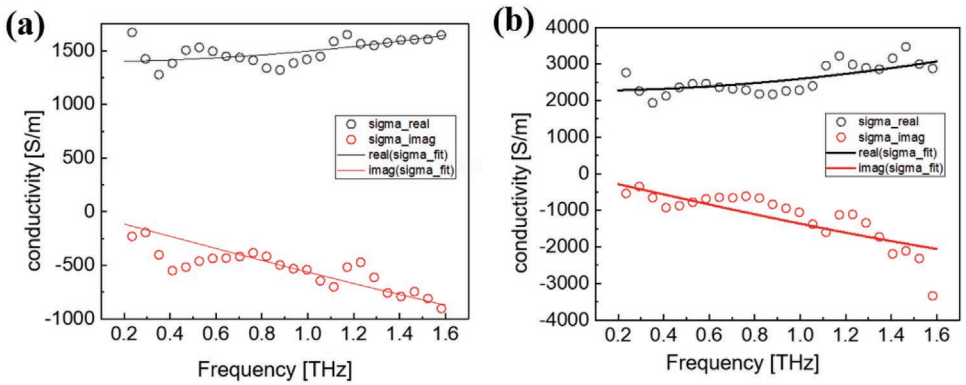

Figure 3. THz conductivity spectra of a) Vib-0 and b) Vib-80 at a pump–probe delay of 5 ps after excitation at 400 nm with a fluence of 113.32 μJ cm^{-2}.

and theoretical calculations for materials with similar compositions.[55,57,58] The frequency of plasma can further be described by a function of the density of charge carriers N

$$\omega_p = \sqrt{\frac{e^2 N}{\varepsilon_0 m^*}} \tag{2}$$

where e is the elementary charge. The real part of the electrical conductivity σ_{DC} is shown as

$$\sigma_{DC} = \frac{e^2 N \tau_s}{m^*}(1+c) \tag{3}$$

The fitting details are listed in **Table 2**, while the results of charge-carrier mobility are presented in **Figure 4**a.

In Table 2, the momentum-relaxation time τ_s for Vib-80 is slightly higher than Vib-0, indicating reduced trap density. As for the charge-carrier density N, our results agree with the range of previous data, and with such a level for charge-carrier density, the bimolecular and Auger recombination processes begin to contribute to the majority of total decay rate.[59] According to the relation of carrier mobility provided before, we infer that $\mu = \sigma_{DC}/(e \cdot N)$. The calculated carrier mobility increases from 89 ± 25 cm^2 V^{-1} s^{-1} for Vib-0, to 121 ± 44 cm^2 V^{-1} s^{-1} for Vib-80. A comparison of carrier mobility for the organic, inorganic, and hybrid perovskites with similar composition is summarized in Table S3 (Supporting Information). The mobility for Vib-0 measured in this work falls within the range between organic and inorganic perovskite thin films, and is reasonable for samples probed on a short length scale.[57] Notably, the carrier mobility of Vib-80 exceeds that of other polycrystalline organic–inorganic hybrid perovskite thin films of similar composition by ≈80 ± 40 cm^2 V^{-1} s^{-1}.[60–63] From the results of charge-carrier density and fitting of THz conductivity transient, we can further obtain the diffusion length for both films. The calculation details are included in the Supporting Information. As shown in Figure 4b, the diffusion length is improved by nearly 1.5 times under various charge-carrier concentrations. The improved carrier lifetime, mobility, and diffusion length contribute to the enhancement in device performance. For example, the incident photon-to-current conversion efficiency of perovskite solar cells was improved up to 90% between 350 and 750 nm subjected to ultrasonic vibration post treatment.[39]

In the foregoing sections, we have shown that ultrasonic vibration has multiple positive effects on the properties of perovskite films. First, the density of trap states is reduced with proper vibration duration. Based on the studies from the PL spectroscopy, we propose a model as demonstrated in **Figure 5**. When the ultrasonic vibration is applied, the intensity of trap state emission is effectively suppressed. This positive effect is also revealed by the extension of carrier lifetime for the TRPL and THz conductivity transients under different excitation fluences, as well as the slight increase in the momentum relaxation time τ_s. According to the X-ray diffractograms (XRD) in Figure S7 (Supporting Information), the films with vibration show an accumulation of residual lead iodide (PbI_2), which can reduce trap states and thus suppress charge-carrier recombination rate, as reported elsewhere.[64–66] In addition, we note that the carrier lifetime up to microseconds was found in the films with pure ultrasonic vibration without annealing, whereas further annealing for 45 min creates defects and significantly reduces the carrier lifetime. Ultrasonic vibration can generate local heating in the film. The temperature of perovskite thin-film surface increased up to 40 °C after 3 min vibration;[42] while for the annealing process at 100 °C the surface temperature was found to be up to 78 °C.[67] The heat generated during the annealing process is much higher in comparison with annealing-free ultrasonic vibration. Our results indicate that ultrasonic vibration post treatment can prevent the defect

Table 2. Plasma frequency (ω_p), momentum relaxation time (τ_s), localization degree (c), charge-carrier density (N), real-part electroconductivity (σ_{DC}), and mobility fitted to the data of electrical conductivity of thin films processed with different vibration times.

Vibration time [s]	ω_p [10^{14} Hz]	τ_s [fs]	c	N [10^{17} cm^{-3}]	σ_{DC} [10^3 S m^{-1}]	Mobility [cm^2 V^{-1} s^{-1}]
0	3.00 ± 0.66	12.6 ± 4.2	−0.86 ± 0.04	9.85 ± 2.61	1.40 ± 0.14	88.8 ± 25.2
80	3.42 ± 0.13	17.1 ± 3.1	−0.87 ± 0.06	11.8 ± 4.25	2.27 ± 0.13	121 ± 43.8

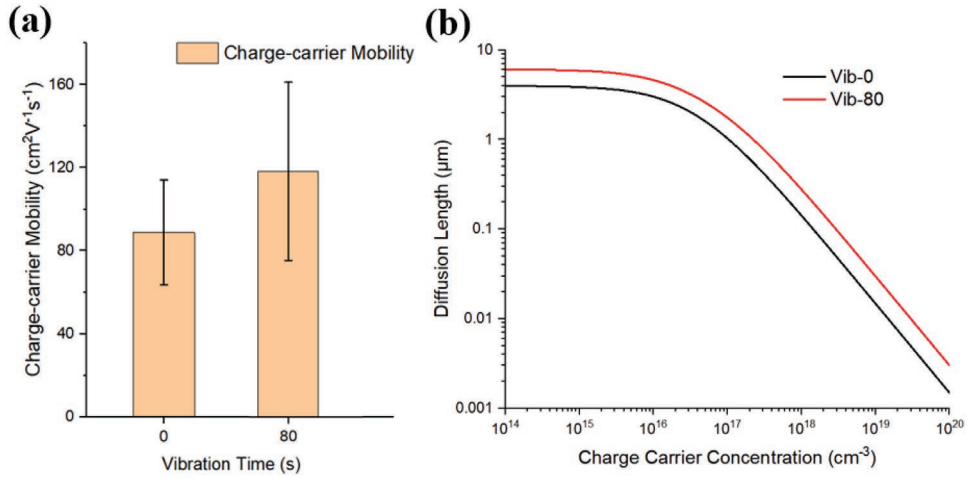

Figure 4. a) Charge-carrier mobility and b) charge-carrier diffusion lengths as a function of charge-carrier concentration for Vib-0 and Vib-80 films.

formation in the perovskite films during the high-temperature annealing process. Therefore, developing an annealing-free or gentle annealing procedure based on ultrasonic vibration at different frequency and amplitude may enhance the device performance.

Second, the mobility of Vib-80 is higher than Vib-0. The carrier mobility is determined by both extrinsic and intrinsic factors. The extrinsic factors include material imperfections such as grain boundaries and impurities. As demonstrated in Figure S8 (Supporting Information), comparing Vib-80 with Vib-0, the variation in average grain size is within their standard deviation. Therefore, it is likely that the intrinsic factors, originated from the interactions between charge carriers and lattice or phonons, play a more important role in the increased mobility. Theoretical and experimental studies have shown that a critical factor that limits the charge-carrier mobility for MHPs at room temperature is the Fröhlich coupling with longitudinal–optical phonons.[68–70] The XRD patterns in Figure S7 (Supporting Information) reveal shifts in peak positions, implying possible difference in phonon modes or frequencies when different vibration times are imposed. Such peak shifts may originate from the increase of FA^+/MA^+ or Br^-/I^- ratios as a result of ion migration,[39,71,72] or changes in the interplanar distances induced by compressive strain.[73] The increase in compressive strain could be one of the reasons that change the grain size when the vibration time is increased to 100 s, as shown in Figure S8 (Supporting Information). Further research on vibration-induced effects on the electron–phonon coupling is expected to unravel more details of composition and crystal structure changes induced by ultrasonic vibration, thus offers a better understanding of the factors that limit the charge-carrier mobility.

3. Conclusion

In summary, we have studied the effects of ultrasonic substrate vibration post treatment on the carrier lifetime and mobility of triple-cation perovskite thin films. Comparing to the thermal annealed films, the average carrier lifetime increases up to 2 orders of magnitude for the films subjected to 80 s of annealing-free vibration, indicating a decrease in carrier trapping rate, while defects are created during the postannealing procedure. Under postannealing condition, OPTP spectroscopy reveals that the charge-carrier mobility for the films treated with 80 s of ultrasonic vibration reaches 121 ± 44 cm^2 V^{-1} s^{-1}, about 80 ± 40 cm^2 V^{-1} s^{-1} higher than other polycrystalline organic–inorganic hybrid perovskite thin films of similar composition. The films treated with vibration also showed longer charge-carrier diffusion length. Our results suggest that through the

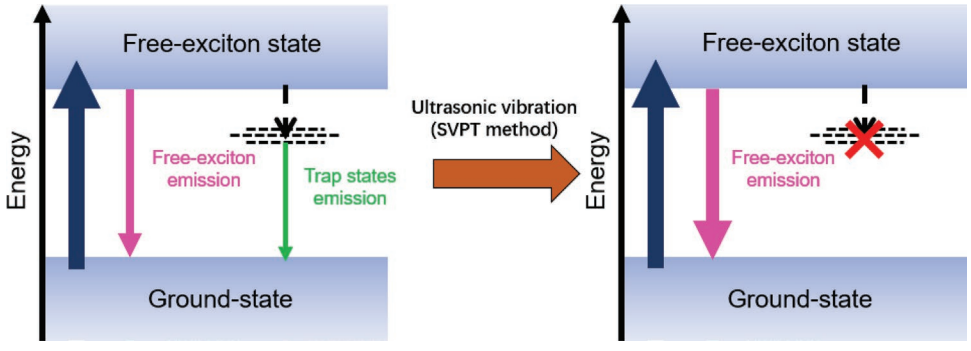

Figure 5. Proposed band diagram and emissions affected by ultrasonic substrate vibration post treatment. After the application of ultrasonic vibration, the trap states are suppressed, thus reducing the trap states emission.

ultrasonic vibration post treatment, the charge-carrier recombination in perovskite crystals is effectively suppressed, leading to a significantly improved charge-carrier lifetime. This work will motivate further development on an annealing-free or gentle annealing procedure for the perovskite films based on ultrasonic vibration, aiming at significantly improving the performance of perovskite electronic devices.

4. Experimental Section

Materials: Materials used in this paper included zinc nitrate hexahydrate ($Zn(NO_3)_2{\cdot}6H_2O$, 99%, Sinopharm Chemical Reagent Co., Ltd.), methylammonium iodide (CH_3NH_3I, 99.5%, Xi'an Polymer Light Technology Corp.), PbI_2 (99.9%, Xi'an Polymer Light Technology Corp.), lead bromide ($PbBr_2$, 99.9%, Xi'an Polymer Light Technology Corp.), formamidinium iodide ($CHNH_2NH_2I$, 98%, Xi'an Polymer Light Technology Corp.), cesium iodide (CsI, 98%, Xi'an Polymer Light Technology Corp.), chlorobenzene (CB, 99.9%, Sigma–Aldrich), 2-methyl imidazole (2-mIm, 99%, Sigma–Aldrich), dimethylformamide (DMF, 99.8%, Sigma–Aldrich), and dimethyl sulfoxide (DMSO, 99.9%, Sigma–Aldrich).

Sample Preparation: All glassware including brown bottles, *z*-cut quartz, and fluorine-doped tin oxide (FTO) glass substrates were placed in an ultrasonic cleaner, processed by detergent, ethanol (99.9%), and acetone (99.9%) sequentially, and cleaned for 15 min. After that, the bottles were placed on a heater setting at 100 °C so as to evaporate the remaining acetone. In the meantime, the substrates were processed under UV light for 20 min to further clear up the acetone around them.

To study the charge-carrier lifetime, triple-cation perovskite films were deposited on *z*-cut quartz substrates sized 1 cm × 1 cm without any electron- or hole-transport layer. Prior to the deposition of perovskite films on quartz substrates, ZIF-8 was applied, where ZIF stands for zeolitic imidazolate frameworks, to improve the crystallinity of grains. This strategy was proved effective by Shen et al.[74] To synthesize ZIF-8, a methanolic solution of 2-mIm (0.660 g in 15 mL of methanol) was added to a methanolic solution of zinc nitrate (0.297 g in 15 mL of methanol), followed by stirring at room temperature. After synthesis, the solution was spun on the surface of quartz glass at 1500 rpm for 30 s. All samples were dried at 50 °C for 10 min.

To prepare the precursor solution for triple-cation perovskite, 0.25 g of PbI_2 was dissolved in 0.3615 mL of the mixed solvent system consisting of DMF and DMSO with a volume ratio of 1:4 (denoted as solution A); another 0.25 g of $PbBr_2$ was dissolved in 0.454 mL of the mixed solvent system with the same volume ratio (solution B). Solutions A and B were heated at 180 °C for 10 min, and cooled to room temperature before used in the next step. About 0.025 g of FAI was dissolved in 0.117 mL of solution A (denoted as solution C), and another 0.025 g of MABr was dissolved in 0.176 mL of solution B (denoted as solution D). About 0.200 g of CsI was dissolved in 0.5132 mL of DMSO (named as solution E). 100 µL of C, 20 µL of D, and 4 µL of E were finally fully mixed together, and heated at 55 °C for 12 h, forming the final precursor solution. The spin-coating procedure of triple-cation perovskite films was based on a previous work.[3] The prepared Cs/FA/MA perovskite solution was spun on the ZIF-8 layer for 10 s at 1000 rpm, and then 20 s at 5000 rpm. 250 µL of CB, acting as an antisolvent, was dropped on the film for 15 s after the second step of spin coating had started. The liquid perovskite films were placed on a disk-shaped Langevin ultrasonic transducer, housed by a steel box, at various processing times (0, 20, 40, 60, 80, and 100 s). Following the previous work,[38] the vibration frequency of 40 kHz and the transducer power of 40 W were applied, generating an ultrasonic vibration amplitude of about 7 nm. For convenience, these samples were named as Vib-*x*, where "Vib" stands for word "vibration" and *x* stands for the time (s) of ultrasonic vibration. Finally, all samples were thermal annealed at 100 °C for a time of 45 min according to a previous study.[75] For comparison, one set of thin films was post-treated with 80 s vibration, and not annealed, denoted as "annealing-free vibration." The nominal stoichiometric composition of the thin films was $Cs_{0.05}(MA_{0.17}FA_{0.83})_{0.95}Pb(I_{0.83}Br_{0.17})_3$, given that the only variable parameter was the vibration time, and the amount of reactants consumed to make precursor was unchanged. It was noted that it is possible that the film composition may change after vibration, which requires further study. The annealing post treatment was carried out in order to eliminate the influence of residual solvents, DMF and DMSO, which still remained in the film after vibration.[42] These solvents would form intermediate phases with perovskites. Removing the solvent helps nuclei growth under favorable thermodynamic conditions, and can increase the film conductivity.[42]

Characterization: XRD patterns of the perovskite thin films were recorded on a Bruker D8 advanced diffractometer, applying Cu Kα radiation at a scan rate of 0.1° s^{-1} from 5° to 70°. A confocal laser scanning microscope (LMS700, Zeiss, Germany) was used to obtain the thickness of the perovskite thin film. The morphology of the perovskite film was observed by a field-effect scanning electron microscope (FE-SEM, Zeiss Ultra Plus, Germany) in the Advanced Electronic Materials and Devices (AEMD) Center at Shanghai Jiao Tong University. The SEM images were analyzed using ImageJ software to estimate the grain size distribution. UV–vis absorption spectra were recorded by a UV–vis–NIR spectrophotometer (Lambda 950), over the range of 300–1100 nm. Steady PL and TRPL were measured with an FLS1000 photoluminescence spectroscopy instrument with 405 nm as the excitation wavelength. A time-correlated single-photon-counting (TCSPC) module was used to analyze the TRPL results of the perovskite films probed at 753 nm, where the preset photon count was 2000. For the PL and TRPL measurements, the scan slit and the fixed slit were set to 8 and 7 µm, respectively, unless specified otherwise.

The OPTP spectra were obtained by a regenerative Ti:sapphire amplifier system, producing 2 mJ pulses, a duration of 120 fs, a repetition rate of 1 kHz, and a central wavelength of 400 nm. The laser was split into three beams: two of them were for terahertz generation and detection; and the third one with much higher intensity was used as pump pulse. THz pulses were generated from the femtosecond (fs) laser pulses by optical rectification in a 1 mm thick ZnTe(110) crystal. A pair of off-axis parabolic mirrors were used to collimate and focus the emitted THz radiation onto the top of the test samples. After propagation through the sample, another pair of off-axis parabolic mirrors were used to collimate and focus the diverging THz radiation onto another 1 mm thick ZnTe(110) crystal. The sampling beam was scanned using an optical delay stage. The THz field was detected by free-space electro-optic sampling. The pump beam was scanned using a second optical delay stage that enabled the variation of the time delay of the THz probe pulse with respect to the optical excitation pulse. The pump beam and THz beam were overlapped on the surface of the sample. A lock-in amplifier phase locked to an optical chopper modulating either the THz generation arm or the pump beam arm at a frequency of 500 Hz was used to collect the signal. The spot size of the pump and THz beams were 10 and 3 mm, respectively. All measurements were completed at a temperature of 293 K and relative humidity of less than 18%.

Supporting Information

Supporting Information is available from the Wiley Online Library or from the author.

Acknowledgements

Y.W. and M.-R.A.-Y. contributed equally to this work. Financial support from National Natural Science Foundation of China (Grant Nos. 51802193 and 61975110) is acknowledged. The authors thank Xiao Ling, Peng Du, Yuljae Cho (UM-SJTU Joint Institute), and Chun-Chao Chen (SJTU) for scientific discussions, and four anonymous reviewers for valuable comments and suggestions.

Conflict of Interest

The authors declare no conflict of interest.

Data Availability Statement

The data that support the findings of this study are available from the corresponding author upon reasonable request.

Keywords

carrier mobility, charge-carrier transport, metal halide perovskites, terahertz spectroscopy, ultrasonic vibration post treatment

Received: November 26, 2021
Revised: April 14, 2022
Published online: May 15, 2022

[1] A. Kojima, K. Teshima, Y. Shirai, T. Miyasaka, *J. Am. Chem. Soc.* **2009**, *131*, 6050.
[2] Best research-cell efficiency chart, http://www.nrel.gov/pv/cell-efficiency.html (accessed: June 2021).
[3] M.-R. Ahmadian-Yazdi, N. Gholampour, M. Eslamian, *ACS Appl. Energy Mater.* **2020**, *3*, 3134.
[4] N. Wang, L. Cheng, R. Ge, S. Zhang, Y. Miao, W. Zou, C. Yi, Y. Sun, Y. Cao, R. Yang, Y. Wei, Q. Guo, Y. Ke, M. Yu, Y. Jin, Y. Liu, Q. Ding, D. Di, L. Yang, G. Xing, H. Tian, C. Jin, F. Gao, R. H. Friend, J. Wang, W. Huang, *Nat. Photonics* **2016**, *10*, 699.
[5] Q. V. Le, K. Hong, H. W. Jang, S. Y. Kim, *Adv. Electron. Mater.* **2018**, *4*, 1800335.
[6] L. Dou, Y. M. Yang, J. You, Z. Hong, W.-H. Chang, G. Li, Y. Yang, *Nat. Commun.* **2014**, *5*, 5404.
[7] Y. Guo, C. Liu, H. Tanaka, E. Nakamura, *J. Phys. Chem. Lett.* **2015**, *6*, 535.
[8] C. Y. Wu, W. Peng, T. Fang, B. Wang, C. Xie, L. Wang, W. H. Yang, L. B. Luo, *Adv. Electron. Mater.* **2019**, *5*, 1900135.
[9] H. Gu, S. C. Chen, Q. Zheng, *Adv. Opt. Mater.* **2020**, *9*, 2001637.
[10] H. Zhu, Y. Fu, F. Meng, X. Wu, Z. Gong, Q. Ding, M. V. Gustafsson, M. T. Trinh, S. Jin, X.-Y. Zhu, *Nat. Mater.* **2015**, *14*, 636.
[11] S. A. Veldhuis, P. P. Boix, N. Yantara, M. Li, T. C. Sum, N. Mathews, S. G. Mhaisalkar, *Adv. Mater.* **2016**, *28*, 6804.
[12] Q. Zhang, R. Su, W. Du, X. Liu, L. Zhao, S. T. Ha, Q. Xiong, *Small Methods* **2017**, *1*, 1700163.
[13] H. Kim, J. S. Han, J. Choi, S. Y. Kim, H. W. Jang, *Small Methods* **2018**, *2*, 1700310.
[14] T. Wu, W. Pisula, M. Y. Rashid, P. Gao, *Adv. Electron. Mater.* **2019**, *5*, 1900444.
[15] C. Qin, F. Zhang, L. Qin, X. Liu, H. Ji, L. Li, Y. Hu, Z. Lou, Y. Hou, F. Teng, *Adv. Electron. Mater.* **2021**, *7*, 2100384.
[16] M. Saliba, T. Matsui, J.-Y. Seo, K. Domanski, J.-P. Correa-Baena, M. K. Nazeeruddin, S. M. Zakeeruddin, W. Tress, A. Abate, A. Hagfeldt, M. Grätzel, *Energy Environ. Sci.* **2016**, *9*, 1989.
[17] M. Stolterfoht, C. M. Wolff, Y. Amir, A. Paulke, L. Perdigón-Toro, P. Caprioglio, D. Neher, *Energy Environ. Sci.* **2017**, *10*, 1530.
[18] T. Singh, T. Miyasaka, *Adv. Energy Mater.* **2017**, *8*, 1700677.
[19] T. Singh, S. Öz, A. Sasinska, R. Frohnhoven, S. Mathur, T. Miyasaka, *Adv. Funct. Mater.* **2018**, *28*, 1706287.
[20] N. Li, S. Tao, Y. Chen, X. Niu, C. K. Onwudinanti, C. Hu, Z. Qiu, Z. Xu, G. Zheng, L. Wang, Y. Zhang, L. Li, H. Liu, Y. Lun, J. Hong, X. Wang, Y. Liu, H. Xie, Y. Gao, Y. Bai, S. Yang, G. Brocks, Q. Chen, H. Zhou, *Nat. Energy* **2019**, *4*, 408.
[21] M. De Bastiani, A. J. Mirabelli, Y. Hou, F. Gota, E. Aydin, T. G. Allen, J. Troughton, A. S. Subbiah, F. H. Isikgor, J. Liu, L. Xu, B. Chen, E. Van Kerschaver, D. Baran, B. Fraboni, M. F. Salvador, U. W. Paetzold, E. H. Sargent, S. De Wolf, *Nat. Energy* **2021**, *6*, 167.
[22] K. Gao, J. Miao, L. Xiao, W. Deng, Y. Kan, T. Liang, C. Wang, F. Huang, J. Peng, Y. Cao, F. Liu, T. P. Russell, H. Wu, X. Peng, *Adv. Mater.* **2016**, *28*, 4727.
[23] K. Gao, Y. Kan, X. Chen, F. Liu, B. Kan, L. Nian, X. Wan, Y. Chen, X. Peng, T. P. Russell, Y. Cao, A. K. Y. Jen, *Adv. Mater.* **2020**, *32*, 1906129.
[24] B. Dou, V. L. Pool, M. F. Toney, M. F. van Hest, *Chem. Mater.* **2017**, *29*, 5931.
[25] D. Liu, L. Wu, C. Li, S. Ren, J. Zhang, W. Li, L. Feng, *ACS Appl. Mater. Interfaces* **2015**, *7*, 16330.
[26] J. A. Aguiar, S. Wozny, N. R. Alkurd, M. Yang, L. Kovarik, T. G. Holesinger, M. Al-Jassim, K. Zhu, W. Zhou, J. J. Berry, *ACS Energy Lett.* **2016**, *1*, 155.
[27] M. Kim, G.-H. Kim, K. S. Oh, Y. Jo, H. Yoon, K.-H. Kim, H. Lee, J. Y. Kim, D. S. Kim, *ACS Nano* **2017**, *11*, 6057.
[28] F. X. Xie, D. Zhang, H. Su, X. Ren, K. S. Wong, M. Grätzel, W. C. Choy, *ACS Nano* **2015**, *9*, 639.
[29] C. M. Soe, C. C. Stoumpos, B. Harutyunyan, E. F. Manley, L. X. Chen, M. J. Bedzyk, T. J. Marks, M. G. Kanatzidis, *ChemSusChem* **2016**, *9*, 2656.
[30] F. Michael, *Abstr. Pap. Printed Philos. Trans. R. Soc., London* **1837**, *3*, 49.
[31] S. Kumar, O. K. Matar, *J. Fluid Mech.* **2002**, *466*, 249.
[32] S. Kumar, O. K. Matar, *Phys. Fluids* **2004**, *16*, 39.
[33] O. K. Matar, S. Kumar, R. V. Craster, *J. Fluid Mech.* **2004**, *520*, 243.
[34] S. Shklyaev, M. Khenner, A. A. Alabuzhev, *Phys. Rev. E* **2008**, *77*, 036320.
[35] S. Shklyaev, A. A. Alabuzhev, M. Khenner, *Phys. Rev. E* **2009**, *79*, 051603.
[36] M. Bestehorn, *Phys. Fluids* **2013**, *25*, 114106.
[37] T. Khan, M. Eslamian, *J. Fluid Mech.* **2020**, *900*, 30.
[38] M.-R. Ahmadian-Yazdi, M. Habibi, M. Eslamian, *Appl. Sci.* **2018**, *8*, 308.
[39] H. Xiong, F. Zabihi, H. Wang, Q. Zhang, M. Eslamian, *Nanoscale* **2018**, *10*, 8526.
[40] X. Zhang, F. Zabihi, H. Xiong, M. Eslamian, C. Hou, M. Zhu, H. Wang, Q. Zhang, *Chem. Eng. J.* **2020**, *394*, 124887.
[41] A. Rahimzadeh, M. Eslamian, *Chem. Eng. Sci.* **2017**, *158*, 587.
[42] M.-R. Ahmadian-Yazdi, C. Barratt, A. Rahimzadeh, M. Eslamian, *ACS Omega* **2019**, *5*, 808.
[43] M. Eslamian, *Prog. Org. Coat.* **2017**, *113*, 60.
[44] Y. Xie, F. Zabihi, M. Eslamian, *J. Photonics Energy* **2016**, *6*, 045502.
[45] S. Guo, Y. Zhao, K. Bu, Y. Fu, H. Luo, M. Chen, M. P. Hautzinger, Y. Wang, S. Jin, W. Yang, X. Lü, *Angew. Chem.* **2020**, *132*, 17686.
[46] C.-X. Chen, J. Wang, M. Gao, D. Shi, *Cryst. Growth Des.* **2020**, *21*, 45.
[47] F. Lang, M. Jošt, J. Bundesmann, A. Denker, S. Albrecht, G. Landi, H.-C. Neitzert, J. Rappich, N. H. Nickel, *Energy Environ. Sci.* **2019**, *12*, 1634.
[48] L. Zhang, Y. Liu, X. He, H. Ye, J. Leng, X. Ren, S. Jin, S. Liu, *J. Phys. Chem. C* **2020**, *124*, 22011.
[49] Y. Yamada, T. Nakamura, M. Endo, A. Wakamiya, Y. Kanemitsu, *J. Am. Chem. Soc.* **2014**, *136*, 11610.
[50] Z. Jin, D. Gehrig, C. Dyer-Smith, E. J. Heilweil, F. Laquai, M. Bonn, D. Turchinovich, *J. Phys. Chem. Lett.* **2014**, *5*, 3662.
[51] P. W. Anderson, *Phys. Rev.* **1958**, *109*, 1492.
[52] D. G. Cooke, F. C. Krebs, P. U. Jepsen, *Phys. Rev. Lett.* **2012**, *108*, 056603.
[53] N. Smith, *Phys. Rev. B* **2001**, *64*, 155106.

[54] T. Unuma, N. Yamada, A. Nakamura, H. Kishida, S.-C. Lee, E.-Y. Hong, S.-H. Lee, O.-P. Kwon, *Appl. Phys. Lett.* **2013**, *103*, 053303.
[55] Z. Yang, A. Surrente, K. Galkowski, A. Miyata, O. Portugall, R. J. Sutton, A. A. Haghighirad, H. J. Snaith, D. K. Maude, P. Plochocka, R. J. Nicholas, *ACS Energy Lett.* **2017**, *2*, 1621.
[56] P. D. Cunningham, L. M. Hayden, H.-L. Yip, A. K.-Y. Jen, *J. Phys. Chem. B* **2009**, *113*, 15427.
[57] J. M. Frost, *Phys. Rev. B* **2017**, *96*, 195202.
[58] K. Galkowski, A. Mitioglu, A. Miyata, P. Plochocka, O. Portugall, G. E. Eperon, J. T.-W. Wang, T. Stergiopoulos, S. D. Stranks, H. J. Snaith, R. J. Nicholas, *Energy Environ. Sci.* **2016**, *9*, 962.
[59] C. Wehrenfennig, G. E. Eperon, M. B. Johnston, H. J. Snaith, L. M. Herz, *Adv. Mater.* **2013**, *26*, 1584.
[60] W. Rehman, R. L. Milot, G. E. Eperon, C. Wehrenfennig, J. L. Boland, H. J. Snaith, M. B. Johnston, L. M. Herz, *Adv. Mater.* **2015**, *27*, 7938.
[61] W. Rehman, D. P. McMeekin, J. B. Patel, R. L. Milot, M. B. Johnston, H. J. Snaith, L. M. Herz, *Energy Environ. Sci.* **2017**, *10*, 361.
[62] D. P. McMeekin, G. Sadoughi, W. Rehman, G. E. Eperon, M. Saliba, M. T. Hörantner, A. Haghighirad, N. Sakai, L. Korte, B. Rech, M. B. Johnston, L. M. Herz, H. J. Snaith, *Science* **2016**, *351*, 151.
[63] D. P. McMeekin, Z. Wang, W. Rehman, F. Pulvirenti, J. B. Patel, N. K. Noel, M. B. Johnston, S. R. Marder, L. M. Herz, H. J. Snaith, *Adv. Mater.* **2017**, *29*, 1607039.
[64] C. Wang, C. Zhang, S. Wang, G. Liu, H. Xia, S. Tong, J. He, D. Niu, C. Zhou, K. Ding, Y. Gao, J. Yang, *Sol. RRL* **2018**, *2*, 1700209.
[65] S. Prathapani, D. Choudhary, S. Mallick, P. Bhargava, A. Yella, *CrystEngComm* **2017**, *19*, 3834.
[66] S. Wang, W. Dong, X. Fang, Q. Zhang, S. Zhou, Z. Deng, R. Tao, J. Shao, R. Xia, C. Song, L. Hu, J. Zhu, *Nanoscale* **2016**, *8*, 6600.
[67] M.-R. Ahmadian-Yazdi, M. Eslamian, *Langmuir* **2021**, *37*, 2596.
[68] Z.-G. Yu, *J. Phys. Chem. Lett.* **2016**, *7*, 3078.
[69] A. Filippetti, A. Mattoni, C. Caddeo, M. I. Saba, P. Delugas, *Phys. Chem. Chem. Phys.* **2016**, *18*, 15352.
[70] A. D. Wright, C. Verdi, R. L. Milot, G. E. Eperon, M. A. Pérez-Osorio, H. J. Snaith, F. Giustino, M. B. Johnston, L. M. Herz, *Nat. Commun.* **2016**, *7*, 11755.
[71] Y. Tu, J. Wu, Z. Lan, X. He, J. Dong, J. Jia, P. Guo, J. Lin, M. Huang, Y. Huang, *Sci. Rep.* **2017**, *7*, 44603.
[72] N. J. Jeon, J. H. Noh, W. S. Yang, Y. C. Kim, S. Ryu, J. Seo, S. I. Seok, *Nature* **2015**, *517*, 476.
[73] F. Zabihi, M. Eslamian, *Crystals* **2018**, *8*, 60.
[74] D. Shen, A. Pang, Y. Li, J. Dou, M. Wei, *Chem. Commun.* **2018**, *54*, 1253.
[75] L. Tian, W. Zhang, Y. Huang, F. Wen, H. Yu, Y. Li, Q. Wang, C. Peng, Z. Ma, T. Hu, L. Du, M. Zhang, *ACS Appl. Mater. Interfaces* **2020**, *12*, 29344.